



Load shedding characteristics of an oscillating surge wave energy converter with variable geometry

Michael A. Choiniere^{a,*}, Nathan M. Tom^b, Krish P. Thiagarajan^{c,1}

^a Department of Mechanical Engineering, University of Maine, 5711 Boardman Hall Room 219, Orono, ME, 04469, USA

^b National Renewable Energy Laboratory, MS 3811, 15013 Denver West Parkway, Golden, CO, 80401, USA

^c Department of Mechanical Engineering, University of Maine, 5711 Boardman Hall Room 229, Orono, ME, 04469, USA

ARTICLE INFO

Keywords:

Oscillating surge wave energy converter
Wave energy converter
Load shedding
Variable geometry

ABSTRACT

This study investigates performance and load shedding capabilities of an oscillating surge wave energy converter (OSWEC) that utilizes adjustable geometry to control hydrodynamic coefficients. The body consists of a bottom-hinged rectangular paddle in which the frame holds five horizontal flaps spanning the interior of the frame. Each flap can rotate independently about its center of rotation to alter hydrodynamic coefficients. A 1:14 scale model was built for wave tank tests where the OSWEC's natural response to regular waves was measured. Tests with the paddle fixed vertically were conducted to measure the moment induced by incident waves. Results were compared to numerical simulations which determined that flap orientation significantly affected wave energy transmission past the device. Numerical simulations with the addition of a linear rotational damper power take-off (PTO) suggested that with flaps open, the resistive moment was reduced by up to 47%, the surge force on the foundation up to 55%, and the capture width up to 72% over a range of wave periods and PTO damping values. The experimental nondimensional excitation moments and reflection coefficients were reduced by up to 54%. Overall, the flaps provide mechanical means to reduce loads, thus improving the design life of a WEC system.

1. Introduction

In this paper, we study the performance and load shedding characteristics of a bottom-hinged oscillating paddle with variable geometry. This concept was labeled as an oscillating surge wave energy converter (OSWEC) that had been proposed in (Tom et al., 2016). Coastal and nearshore wave energy converters (WECs), similar to the one proposed here, have been the subject of recent research, with concepts like the Oyster (Whittaker and Folley, 2012), Waveroller (Lucas et al., 2012), and the surge WEC (Ramudu, 2011). Wave-structure interaction studies on similar flap type WECs have been performed looking at the viscous effects (Wei et al., 2015) and slamming (Wei et al., 2016), (Henry et al., 2013). As with all marine structures, the survivability of WECs in extreme environmental conditions becomes a driving factor not only in the structural design but PTO components as well. Economics usually determine the power rating of any given WEC based on site specific design waves, so incident wave energy beyond the rated threshold does not result in more power output. This often requires a shutdown

mechanism to be in place to save the structure from failure and damage when incident wave energy exceeds the design threshold (Cameron and Doherty, 2010). The uniqueness of the present concept is the ability to vary geometrical features to either optimize the power generation or shed hydrodynamic loads, subject to different field locations and environmental conditions. Fig. 1 shows a concept of the OSWEC studied in this work while Table 1 defines the variables associated with Fig. 1. The main body is a plate or a paddle with non-negligible thickness, which is hinged near the seafloor and extends up to the mean water level and is subject to the wave field incident normal to its surface. The main response of the plate is an oscillatory rotation (ϕ) about its hinge, and for still water conditions the paddle surface does not pierce the free surface, which contrasts with other similar studies, e.g. (Gomes et al., 2015), and (Crooks et al., 2016). The flaps located in the lower part of the plate can, in principle, be adjusted to any angle (φ) about their axis of rotation. Both ends of each flap can be capped with circular mounting plates for simple adjustment of angle φ . In theory, this concept parallels modern wind turbine designs, which give the ability to feather the blades to

* Corresponding author.

E-mail addresses: michael.choiniere@maine.edu (M.A. Choiniere), nathan.tom@nrel.gov (N.M. Tom), krish.thiagarajan@maine.edu (K.P. Thiagarajan).

¹ Legal name and permanent address: Krish Thiagarajan Sharman, Department of Mechanical and Industrial Engineering, University of Massachusetts Amherst, 160 Governors Dr. Amherst, MA, 01003. kthiagarajan@umass.edu

maintain rated power. For the purposes of this study, the flap orientation was limited to the closed (0°) and open (90°) configurations only. This change in flap orientation leads to the greatest change in the device's hydrodynamic properties and hence its performance as a wave energy extractor.

The remainder of this paper is organized as follows. Section 2 builds the OSWEC frequency domain pitch equation of motion while describing the various moments that are summed about the paddle hinge. Sections 3 and 4 describe the experimental model and the setup respectively. Section 5 gives a brief overview of the numerical setup as the work has been explained well in a previous work (Tom et al., 2016). Section 6 compares the results from both experiments and numerical simulations, however more effort is devoted to using the complementary features of these two sets of results to understand the device performance. The final section concludes with the authors' suggestions on future work.

2. OSWEC frequency domain pitch equation of motion

The equation of motion of the OSWEC paddle can be determined from first principles. The summation of moments about the paddle hinge are given by:

- Hydrostatic restoring moment, M_h , which is the balance between the effects of gravity and buoyancy (Fig. 1) and for small rotation angles, is given by: $M_h = (\rho g \nabla z_b - W z_g) \phi$. Here ρ is the water density, g is acceleration due to gravity, ∇ is the submerged volume of the device, and W is its weight. z_b and z_g denote the vertical positions of the centers of buoyancy and gravity from the origin of reference, respectively.
- Hydrodynamic radiation moment, M_r , is comprised of an added inertia term and a wave damping term. The added inertia is represented by an added moment of inertia coefficient, A_{55} , and arises from the additional torque from the fluid acting on the structure. The radiation damping arises from wave generation as a result of paddle movement. Hydrodynamic moment has been the subject of considerable discussion in (Ramudu, 2011). The linear hydrodynamic radiation moment can be written as $M_r = -A_{55} \ddot{\phi} - B_{55} \dot{\phi}$, where B_{55} is the wave radiation damping coefficient.
- Incident wave-induced moment, M_w , is a combination of the incident wave-induced pressure acting on the surface of the paddle and wave scattering effect. The wave induced forces and moments are

Table 1

Mass properties and critical dimensions defined in Fig. 1.

Mass, m	25.7 kg
Mass Moment of Inertia, J (about COG)	1.372 kg-m ²
Water Depth, d	0.7 m
Center of Gravity, Z_g	-0.364 m
Center of Buoyancy, Z_b	-0.294 m
Hinge Depth, Z_h	-0.652 m

generally calculated from a boundary element method solver, as described later in Section 4. For small amplitude waves, the moment is normally written as a linear function of the wave amplitude, A .

- Mechanical damping, M_s , is a result of any friction in the bearings at the bottom hinge of the paddle. These effects are usually expressed as the product of a damping coefficient, B_s , and the paddle angular velocity and quantified by free decay tests in air.
- Power take-off (PTO) moment, M_{PTO} , caused by the power take-off system working to absorb and convert energy from the oscillating paddle, is normally written as the product of a damping coefficient, B_{PTO} , and the paddle velocity.

It should be noted that a common practice for marine applications is to include a viscous drag term in the equation of motion of a body. However, a study by Wei et al. (2015) used CFD simulations to examine the viscous effect on a similar bottom-hinged WEC. Wei et al. concluded that the viscous effects are negligible as the radiation and diffraction effects are dominant on paddle motion. For this reason, viscous drag terms were not considered for the present study.

By combining these moments, the equation of motion amenable for frequency domain analysis can be written as:

$$[-\omega^2 (J + A_{55}(\omega)) + i\omega(B_{55}(\omega) + B_s + B_{PTO}) + (\rho g \nabla z_b - W z_g)] \phi_0 = M_w(\omega) \# \quad (1)$$

where J represents the device's pitch mass moment of inertia. This equation is a linearized version of the complete nonlinear formulation of the problem. Refer to the work of (Gomes et al., 2015) for a comprehensive treatment of the latter. Herein it is assumed that the far-field incident wave and the paddle motion response are sinusoidal with frequency ω , and with amplitudes A and ϕ_0 , respectively. A nondimensional response amplitude operator (RAO) can be expressed as:

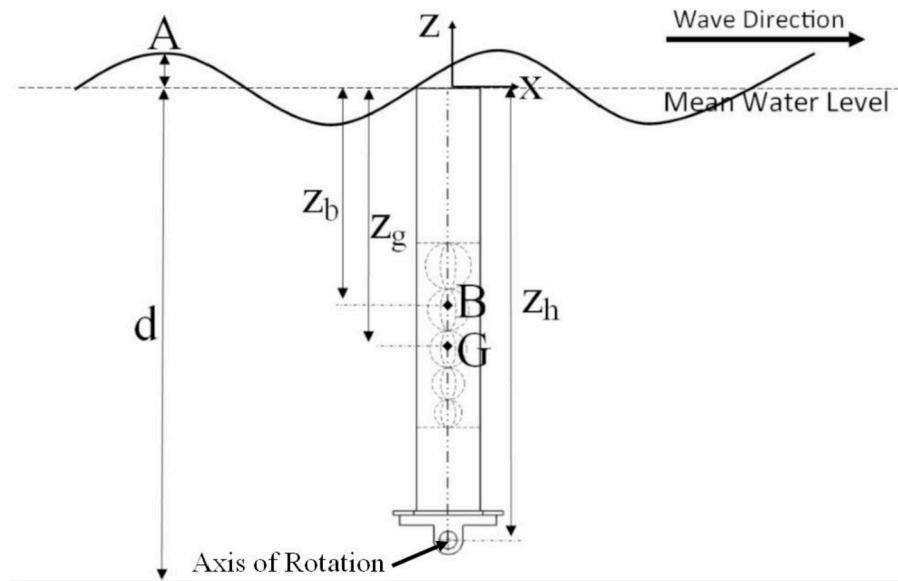


Fig. 1. Side view of the OSWEC device and its associated variables.

$$RAO = \frac{\phi_0}{kA} \# \quad (2)$$

where k is the wave number corresponding to the linear dispersion relation of plane progressive waves and can be computed from the wave frequency and water depth.

Power capture efficiency provides important information regarding the performance of the OSWEC. This concept is explored in this paper using the relative capture width, C_w , which is a ratio of the time-averaged power absorbed by the PTO, P_{TAP} , to the time-averaged power per unit width contained in the incident wave, P_w . From linear wave theory, P_w is obtained from (Wehausen and Laitone, 1960):

$$P_w = \frac{1}{4} \rho g A^2 \sqrt{\frac{g}{k} \tanh kd} \left[1 + \frac{2kd}{\sinh 2kd} \right] \# \quad (3)$$

where d is the water depth. The capture width is nondimensionalized by dividing by the width of the device, w :

$$C_w = \frac{P_{TAP}}{wP_w} \# \quad (4)$$

and referred to as the capture width ratio.

3. Model description

The main paddle of the model under investigation was constructed at approximately a 1:14 scale from sheets of high-density polyethylene that were heat welded at the joints to create watertight, upper and lower hollow chambers connected by solid side plates. Both the upper and lower chambers contained PVC pipes that span the width of the device to act as ballast ports for future studies. These ports were empty and sealed with threaded caps for the current experiments. The main paddle body incorporated a window that housed the variable-pitch flaps. The five variable-pitch elliptical flap cross sections were printed in three dimensions in sections of polylactic acid plastic. The individual sections of each flap were joined with two continuous wooden dowels through the interior of each section spanning the width of the window, and reinforcing strips of fiberglass on each broad side of the ellipse. A final coat of epoxy was applied to protect each flap from leaks. The minor axis dimension of each ellipse is identical for all flaps at 21 mm whereas the major axis dimension is different for each flap as shown in Fig. 2.

The high-density polyethylene body was mounted to a steel bearing plate at its bottom surface and utilized corrosion-resistant bearings with integrated shaft clamps at the locations shown in Fig. 2. Greater detail of the entire device is shown in Fig. 3. The OSWEC was mounted in the wave tank by a rigid frame made of $\frac{1}{4}$ in by 3 in steel flat bar that was clamped to the wave tank structure and hugged the tank walls and floor to create as little obstruction as possible. Finally, a 1-inch-diameter steel shaft connected the OSWEC model to the frame through the bearings.

The OSWEC was free to oscillate about its axis of rotation (ϕ), and each flap can rotate about its respective axis of rotation (φ). This convention is shown in Fig. 1.

4. Experimental methodology

The OSWEC model was tested in an 8-m-long, 1-m-wide wave tank that supports a water depth of 0.7 m. Waves were generated by a vertically actuated wedge of 45° at one end of the tank and a porous beach at the other end to reduce the amplitude of reflected waves. The wave maker and tank can produce regular waves with periods ranging

from 0.6 s to 2.0 s and wave amplitudes of 0.0033–0.0897 m. The width of the OSWEC model was chosen specifically to span the width of the tank to simplify the analysis to two dimensions, assuming water particle motion would be limited to the x - z plane, see Fig. 4.

Prior to installing the OSWEC in the wave tank, wave heights were recorded in the open tank at a sample rate of 1 kHz. The relatively short length of the tank resulted in small wave reflections from the back wall and beach. The interaction between the reflected waves and the motion of the wave maker resulted in small nonlinearities and multiple harmonics in the measured wave elevation. Therefore, a fast Fourier transform (FFT) was used to isolate the wave amplitude of the first harmonic in the data for each set of wave maker inputs. Due to the high sampling rate used in the data acquisition, no special windowing was needed, as the position of the maximum value of the amplitude spectrum correlated with the wave frequency very well. This amplitude is designated as the incident wave amplitude corresponding to the data set and used as inputs for the numerical simulations of the first experiment described below.

Two opposing string potentiometers, each with a 1-m stroke, were used to measure the model OSWEC response in waves. The string potentiometers were mounted to the top tank rail support while the free ends of each string were attached to a vertical steel stanchion that was bolted to the side of the OSWEC. A schematic of the experimental setup is shown in Fig. 4, and a photo of the OSWEC and string potentiometers is shown in Fig. 5. Although the potentiometers measured a linear displacement, the height of the potentiometers above the axis of rotation, H , was considered constant due to a small angle assumption of the paddle motion for the wave conditions tested. Therefore, the rotational displacement, ϕ , of the device was calculated as $\phi = \tan^{-1} \frac{\Delta x}{H}$.

Next, the paddle was fixed vertically to measure the moment about the shaft induced by incident waves in both flap configurations. A rigid vertical stanchion was added at the center of the paddle's width, extending up to the height of the top tank rails. A rigid beam was clamped across the top tank rails and a load cell was bolted between the stanchion and beam, holding the paddle fixed vertically. Maintaining the pinned connection at the shaft, the total moment induced by waves could be measured from the horizontal force recorded at the load cell and the given geometry. Comparing the results between open- and closed-flap cases in this arrangement provided some insight into the load shedding capabilities of the flaps. The reflection coefficient was also calculated in this configuration to show how energy is reflected or transmitted past the device. Fig. 6 shows the setup for this experiment.

Since the fixed paddle resembled a vertical wall spanning the width of the tank, partial standing waves were observed between the paddle and wave maker which warranted further investigation on the incident wave characteristics. The presence of standing waves contaminated the wave field and wavemaker interaction, therefore it was important to separate the incident and reflected waves for calculation of the non-dimensionalized wave-induced moment on the paddle. The composite wave was separated into incident, a_i , and reflected, a_r , amplitude components using the wave record from two fixed probes on the wavemaker side of the paddle (Nallayarasu et al., 1995), (Dean and Dalrymple, 1991) such that

$$a_i = \frac{1}{2|\sin \Delta_2|} \sqrt{A_1^2 + A_2^2 - 2A_1A_2 \cos(\Delta_2 + \delta_2)} \# \quad (5a)$$

$$a_r = \frac{1}{2|\sin \Delta_2|} \sqrt{A_1^2 + A_2^2 - 2A_1A_2 \cos(\Delta_2 - \delta_2)} \# \quad (5b)$$

Table 2

Dimension values (mm) corresponding to Fig. 2.

1	2	3	4	5	6	7	8	9	10	11
66.9	60.0	53.3	46.7	40.0	939.8	900.8	609.8	266.9	651.96	171.95

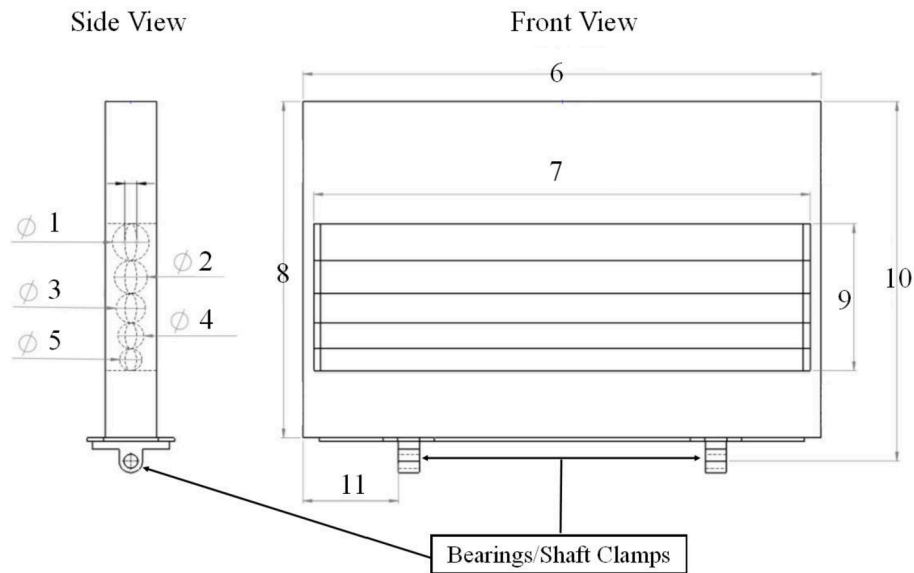


Fig. 2. Dimensions of interest of the scale model OSWEC with variable flaps at $\phi = 0^\circ$. See Table 2 below for corresponding values.



Fig. 3. The OSWEC model exploded in assembly view (left) and the device installed in the wave tank (right).

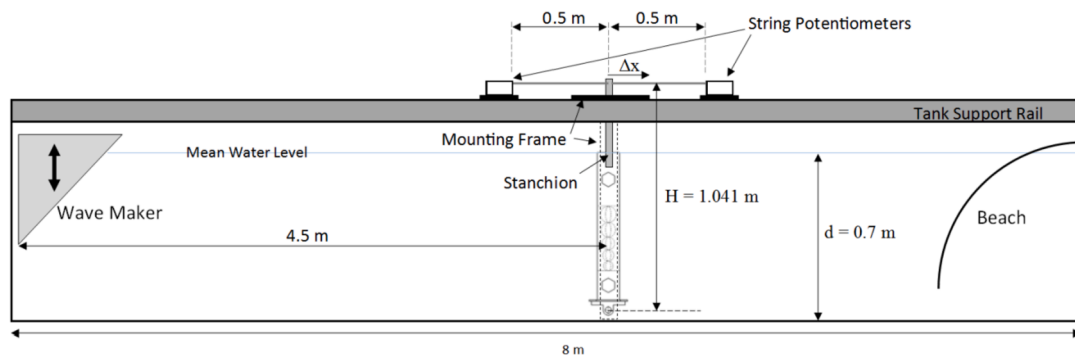


Fig. 4. Wave tank and experimental setup (not to scale).

A_1 and A_2 represent the composite wave amplitude at the first and second wave probes, respectively, δ_2 represents the distance between the two probes, and $\Delta_2 = k\delta_2$, where k is calculated using linear wave theory and the prescribed wavemaker period. Data was collected for approximately 60 s in each run of the fixed-paddle experiments. A_1 and A_2 were determined by separating each dataset into bins of ten wave cycles each where a fast Fourier transform of the time history revealed the amplitude at the dominant frequency. This dominant amplitude in each bin was averaged across all bins in each run and considered as the composite amplitude. Since three probes were installed on the wave-maker side of the paddle, the dominant mode amplitude for each of two

pairs was averaged for further consideration (WP0 – WP1 and WP1 – WP2), refer to Fig. 6. Special care was taken where δ_2 was equal to an integer multiple of half a wavelength, a condition where this method fails. The horizontal force at the load cell was measured using the same method of averaging FFT on bins of ten cycles each. In the previous experiment described above where the paddle was free to oscillate in the generated wave field, the same reflection analysis described here showed that the waves reflected off the paddle interacting with the cyclical motion of the wave maker had negligible impact on the incident wave characteristics when compared to the calibration runs in the open tank. Reflection analysis of the fixed-paddle experiments, however,

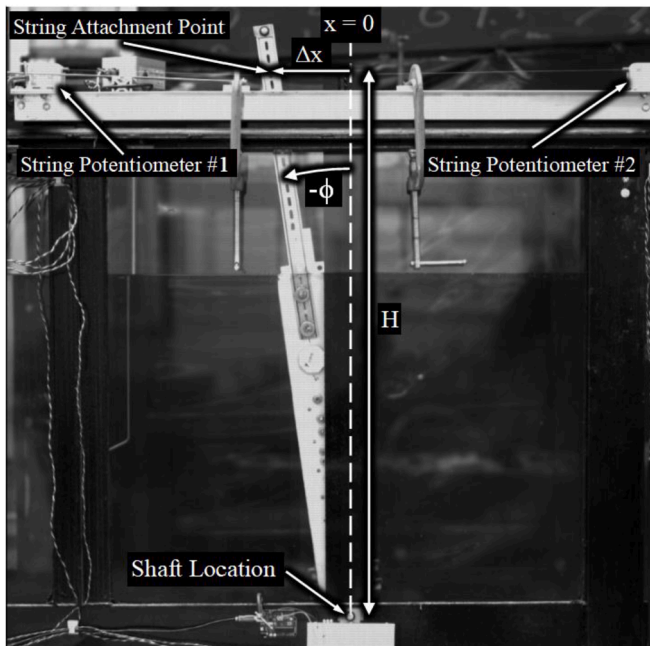


Fig. 5. Instrumentation detail for tracking paddle motion. The two string potentiometers are fixed to the top tank rail at a vertical distance of $H = 1.041$ m from the axis of rotation, and ± 0.5 m in the x -direction from the paddle's neutral vertical position. The free ends of the string potentiometers are attached to the rigid stanchion at the same vertical height, H , from the axis of rotation. The distance Δx is the direct measurement from the string potentiometers.

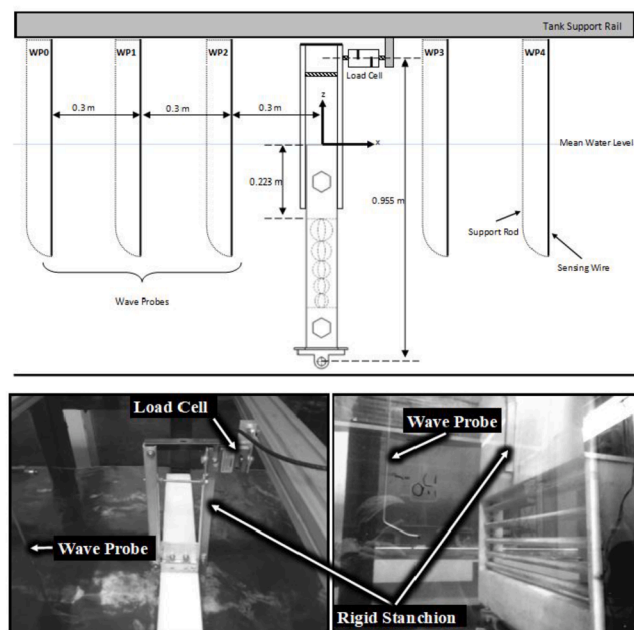


Fig. 6. Experimental setup for the fixed-paddle wave-induced moment and reflection coefficient measurements.

showed that with most wave cases tested the differences between calculated incident wave amplitudes and those wave amplitudes recorded in the calibration runs were no longer negligible. For this reason, the incident wave amplitudes after reflection analysis were considered to be the input waves for corresponding numerical comparisons.

The wave-induced moment about the shaft was calculated simply by multiplying the horizontal force at the load cell by the moment arm of 0.955 m. This moment was nondimensionalized by τ_m , the moment due

to hydrostatic pressure on one side of the paddle.

$$\tau_m = \frac{1}{6} \rho g w d^2 a_i \# \quad (6)$$

Here, w is the width of the paddle. Finally, the reflection coefficient, R_c , was calculated as

$$R_c = \frac{a_r}{a_i} \# \quad (7)$$

5. Numerical simulations

The program selected to predict the OSWEC angular displacement during model tests was WEC-Sim (Ruehl et al., 2014). WEC-Sim is an open-source wave energy converter simulation tool that is built on the MATLAB/SIMULINK framework and arose out of a collaboration between the National Renewable Energy Laboratory and Sandia National Laboratories. Simulations are performed in the time domain by solving the WEC equations of motion in all 6 degrees of freedom. Before WEC-Sim could be run, it was necessary to obtain the mass and hydrodynamic properties of the OSWEC. The translational mass, center of gravity, and mass moment of inertia (see Table 1) were obtained from dry tests at the University of Maine's Advanced Structures & Composites Center. A static angle test was used to find the center of gravity where the device was hung by a single cable at one attachment point. The projection of the static vertical cable was recorded through the device. The device was then hung by two additional attachment points separately, again recording the projected vertical line through the device. The intersection of the three projected lines determined the location of the center of gravity. The mass moment of inertia was calculated by a simple swing test in which the OSWEC's shaft was rigidly secured at both ends, allowing the paddle to hang upside-down and oscillate freely when given an initial displacement. Using an initial offset of approximately 20° from vertical, the paddle was released, and the natural period of oscillation was recorded. Given the measured mass, center of gravity distance to the axis of rotation, and natural period, the moment of inertia was calculated about the axis of rotation. The parallel axis theorem was then used to calculate the moment of inertia about the center of gravity as required by WEC-Sim. The hydrodynamic coefficients were obtained from WAMIT v7.2 ("WAMIT Version 7.2 User Manual," 2017), which now includes the option to analyze bodies in channels with parallel walls. The hydrodynamic coefficients were calculated at a spacing of 0.1 rad/s for wave frequencies between 2.0 rad/s and 11.0 rad/s for the 0° and 90° flap orientations.

The amplitude and frequency of the first harmonic of the wave motion, measured during the open tank tests, were used as the environmental inputs to WEC-Sim. Simulations were run for 40 wave periods (40T), with a time step of $T/100$, a ramp time of 10 wave periods (10T) and using a 4th order Runge-Kutta fixed time-step solver. WEC-Sim has two options to calculate the linear hydrodynamic radiation moment: 1) the sinusoidal steady-state response, which assumes that the added moment of inertia and the wave damping are constant at the simulated wave frequency, and 2) with the full wave radiation convolution integral. However, WAMIT currently does not calculate the infinite frequency added moment of inertia when using the channel option, which prevents simulation using option 2. As a result, option 1 was selected for initial comparisons. The WEC-Sim simulations relied on the linear hydrodynamic forces and no linear or quadratic viscous drag terms were modeled.

A rotational constraint was used in WEC-Sim to model the connection between the OSWEC and the rigid frame shaft. The rotational constraint is required because WEC-Sim requires the mass and hydrodynamic properties to be defined about the center of gravity of each body. It was assumed in the simulations that linear wave theory is applicable and no additional modeling features were used in WEC-Sim. Fig. 7 shows the surge hydrodynamic coefficients from simulations,

which have the greatest effect on the pitch motion of the paddle about the rotational shaft. The nondimensional wave angular frequency is defined as:

6. Results and discussion

Free-decay experiments were performed to identify the damped natural period of the device. Five tests at each flap orientation were recorded and showed sufficient repeatability in response. The string potentiometers used to measure paddle displacement consisted of a fixed case that contains a rotational transducer with an extendable stainless-steel wire rope that attaches to the moving paddle. An internal torsional spring maintains a constant tension on the wire rope throughout its stroke and acts as the retraction mechanism. A lubricated dust wiper makes contact with the wire rope as it extends and retracts in and out of the case creating low friction on the paddle. While the string potentiometers impose a slight mechanical damping force to the paddle in experiments, the operational device would be absent of this force and was low enough to be neglected for these experiments. As shown in Fig. 8, the 0° flap orientation exhibits an irregular decay curve. This irregular decay is likely due to the OSWEC device spanning the width of the tank and hence causing a damming effect. The motion of the displaced water and its reflection on either side wall can thus result in a non-sinusoidal reaction force imposed on the paddle. However, when the flaps are open there is sufficient water movement from one side of the paddle to the other and hence the curve follows the familiar decay pattern.

The damped natural period between the second and third peaks of the 0° flap case was $T_d = 6.73$ s, and $T_d = 4.11$ s in the 90° case. Because the hydrostatic restoring coefficient and pitch mass moment of inertia are constant with flap rotation, the reduction in the damped natural period confirms that the added moment of inertia has been reduced in the 90° case. After scaling up from the 1:14 model results, the full scale damped natural periods are equivalent to $T_d = 25.18$ s and $T_d = 15.38$ s, respectively.

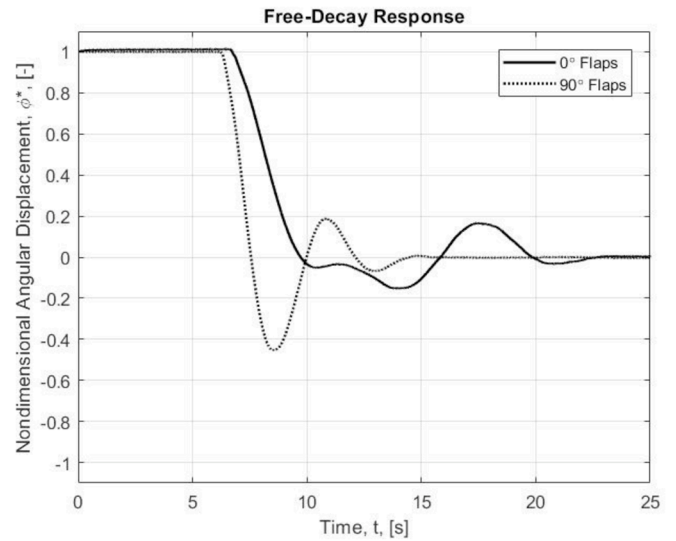


Fig. 8. Free-decay response of the OSWEC when all flaps are oriented in the 0° and 90° flap orientations. The angular displacement was nondimensionalized by the initial offset angle of 10° and referred to as ϕ^* .

Note that the wave maker used in the current experiments is limited to wave periods of 2 s or less, so the device’s response was not examined in waves with periods near these damped natural periods. Much like the wave data collected prior to device installation, the OSWEC’s response to incident waves exhibited multiple harmonics in the angular displacement time history. To be consistent with the method used to characterize the incident wave amplitude, a fast Fourier transform analysis was also performed on the angular displacement time history collected in each run. The amplitude of the first harmonic was considered as the OSWEC’s angular displacement amplitude and used to determine the pitch RAO. The experimental pitch RAO calculations are

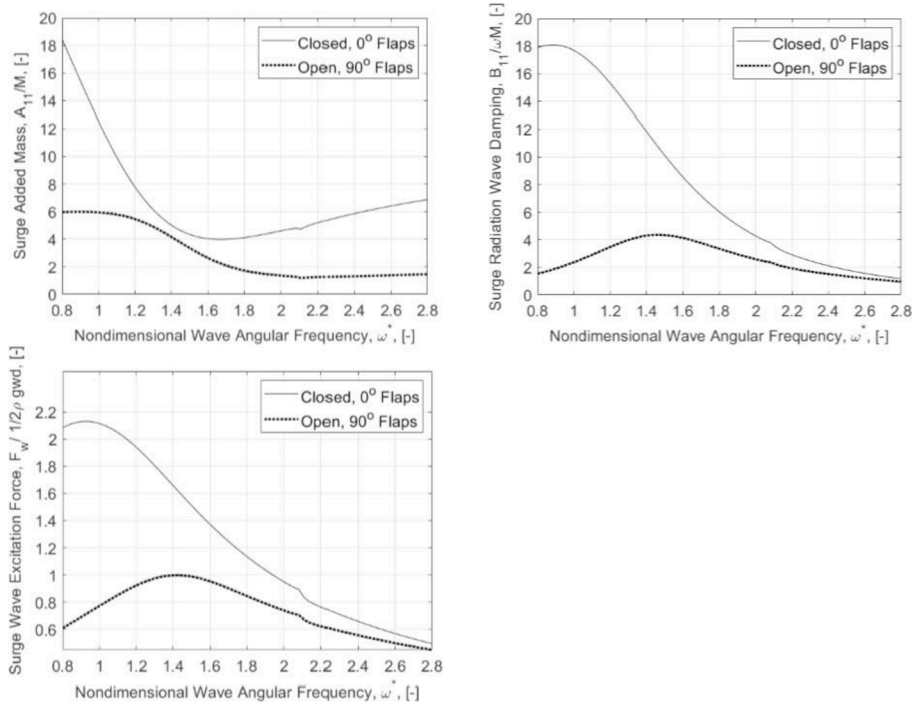


Fig. 7. Surge added mass (top left), surge radiation wave damping (top right), and surge wave excitation force (bottom) as calculated by WAMIT. WEC-Sim requires the hydrodynamic coefficients to be calculated about the center of gravity of the WEC. After placing a revolute joint at the base of the OSWEC, to model the shaft connection, the dominant overturning moment will be generated by the surge hydrodynamic coefficients.

compared to the WEC-Sim results in Fig. 9 and Fig. 10 shows a sample FFT analysis of the paddle's response. The agreement between experiments and simulations are quite apparent in Fig. 9 for the range of frequencies tested.

The numerically derived hydrodynamic coefficients shown in Fig. 7 and the experimental free-decay test shown in Fig. 8 suggest that hydrodynamic properties and the resonant pitch frequency can be adjusted by changing flap orientation. Therefore, the response at each flap orientation was expected to show differences. However, Fig. 9 shows that the flap orientations investigated do not significantly influence the natural (no PTO) OSWEC's pitch response in the environment studied. The experimental wave frequencies tested were likely high enough such that the hydrodynamic wave pressure did not penetrate to the depth of the flaps in this configuration. The pitch displacement magnitude response; however, shows good agreement between the numerical and experimental results, which provides confidence in the hydrodynamics.

While the natural pitch response in waves did not show significant changes between the 0° and 90° flap cases, the differences in free-decay response and hydrodynamic coefficients calculated in WAMIT warranted further investigation of the device's ability to extract energy and shed loads. A linear rotational damper PTO was added to the WEC-Sim model and simulations were performed for wave periods of 0.7, 1.0, 1.3, 1.6, and 1.9 s and PTO damping coefficients ranging between 25 and 425 kg m²·s⁻¹. The WEC-Sim results for the resistive torque applied by the rotational PTO, as a function of the PTO damping coefficient, are shown in Fig. 11.

Another factor that becomes increasingly important as the device approaches full-scale deployment is the load on its foundation. The surge foundation force was examined in WEC-Sim runs with the incorporated rotational PTO. Based on previous numerical studies of the OSWEC's performance (Tom et al., 2016), it can be shown that the foundation reaction force results from both the wave-excitation force and the motion of the paddle. The resulting nondimensional surge force on the supporting frame is shown in Fig. 12. Finally, WEC-Sim was used to estimate the relative capture efficiency of the OSWEC at both the 0° and 90° flap orientations over the same range of PTO damping coefficients with results plotted in Fig. 13. The results from WEC-Sim, shown in Figs. 11–13, demonstrate the ability of the adjustable flap orientation to control PTO and foundation loads.

The wave energy absorption was investigated further using data collected in the experiments previously described. Fig. 14 and Fig. 15 show time histories of the wave field upstream and downstream of the device along with the OSWEC's pitch response, ϕ^* , for wave periods of 1.0 s and 1.6 s (nondimensional wave frequencies of $\omega^* = 1.68$ and $\omega^* = 1.05$, respectively). The pitch response was converted to a length dimension to compare to wave amplitude by $\phi^* = Z_h \tan(\phi)$, where Z_h is the height of the paddle. The time, t , was nondimensionalized by the

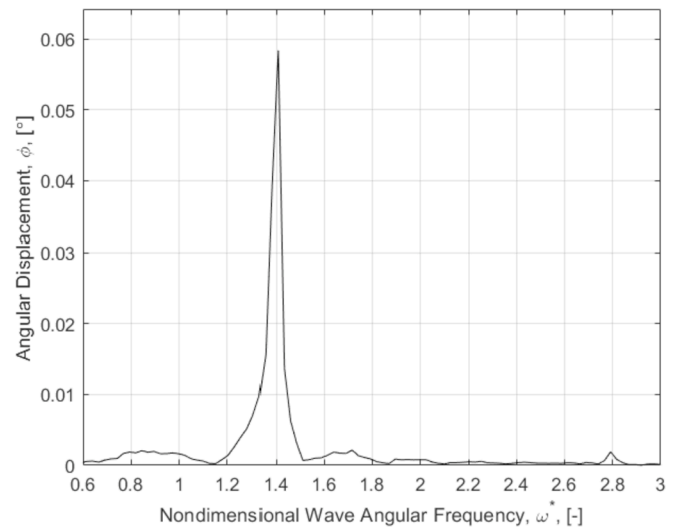


Fig. 10. Sample FFT analysis of the OSWEC's response with closed flaps in regular waves of $T = 1.2$ s and $A = 0.033$ m as measured in the wave tank.

wave period and labeled t^* . The OSWEC was located at $x = 0$ m and the upstream and downstream wave probes were located at $x = -0.53$ m and $x = 0.60$ m, respectively. The horizontal dashed lines represent the intended wave elevation at the paddle location had the device not been installed.

The wave elevation at the upstream probe in each 0° case was greater than the 90° case for the same wave environment. This outcome was expected as the 90° case would allow some of the wave energy to pass through the openings in the flap window which indicates that the device reflects more energy back in the 0° case. Given this information, it would be expected that the 0° flap orientation would radiate a greater amount of energy in the downstream direction. However, the wave elevation at the downstream probe for each wave period does not appear to change between the 0° and 90° flap orientations.

A high-speed camera was used during the experiments to capture nonlinear wave-structure interactions that would help identify differences between the experimental and numerical results. Fig. 16 shows a series of snapshots that highlight an overtopping sequence over one half-period of OSWEC oscillation recorded with the flaps open in a wave period of 1.2 s and a wave amplitude of 0.07 m. As the wave passes the OSWEC, the wave field, radiated and diffracted, on both sides of the paddle can be seen in Fig. 16 as the wave appears to split over the device. Some of the transmitted wave energy is dissipated as the elevated water on each side of the paddle finally collides and projects vertically, as shown in Fig. 16. This vertical projection of the wave surface is a

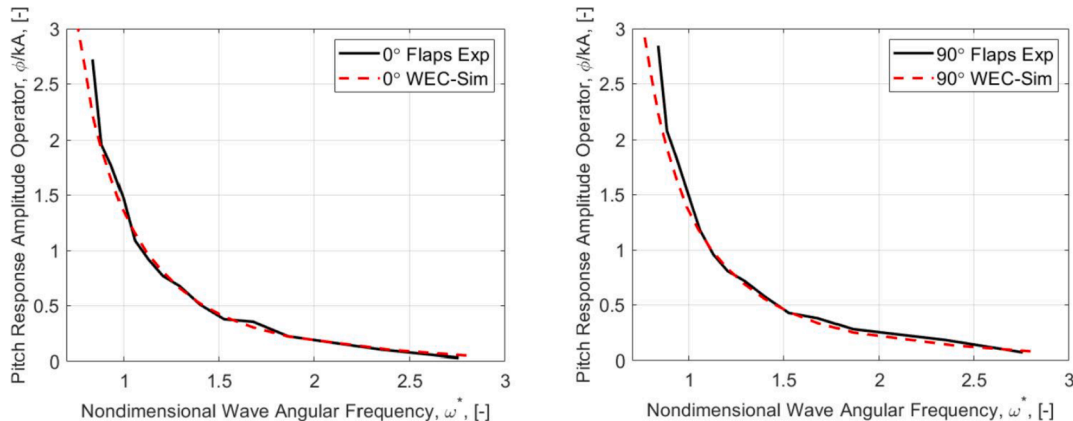


Fig. 9. Pitch RAO calculated from experimental results and WEC-Sim results at both 0° (left) and 90° (right) flap orientations.

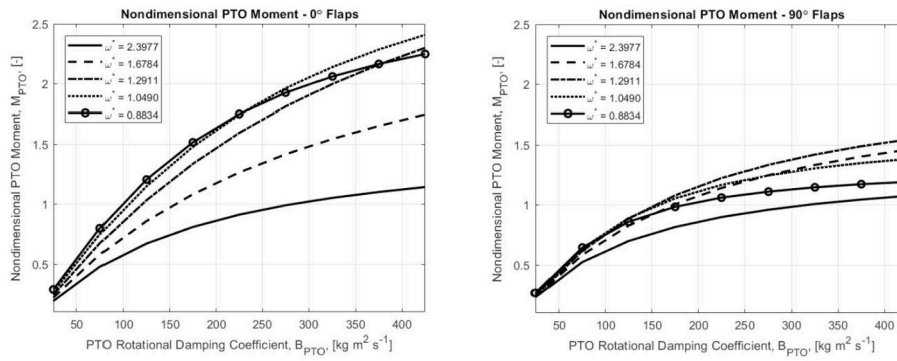


Fig. 11. Nondimensional PTO moment over a range of PTO damping coefficients for both 0° (left) and 90° (right) flap orientations as calculated from simulations. The PTO moments are nondimensionalized by τ_m (Eq. (6)).

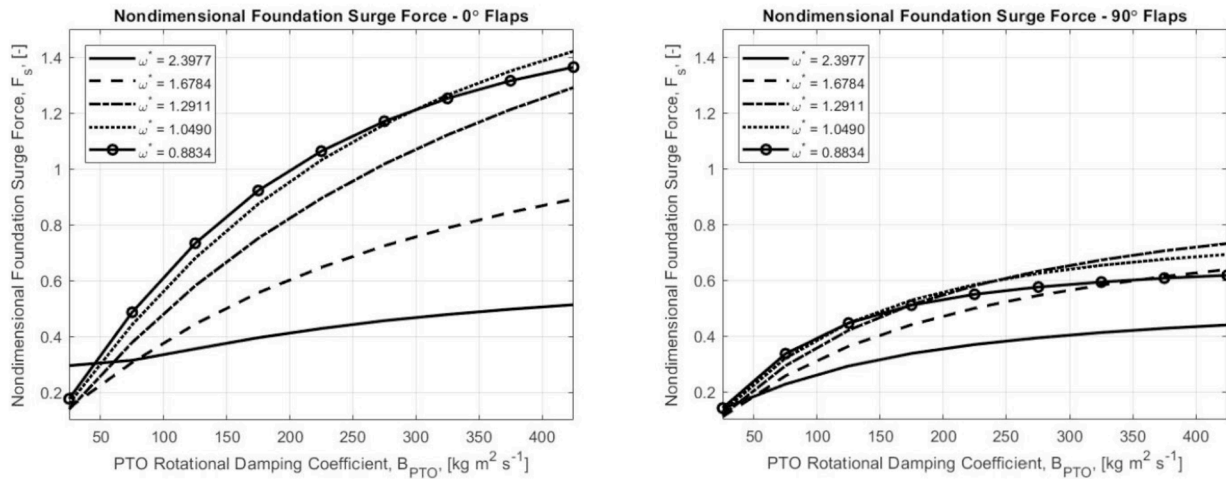


Fig. 12. Nondimensional surge force, F_s , on foundation over a range of PTO damping coefficients for both 0° (left) and 90° (right) flap orientations. The surge forces were nondimensionalized by $f_r = 1/2\rho g w d a_i$, where w is the width of the device. The nondimensional value f_r represents the hydrostatic horizontal force from having water on only one side of the paddle.

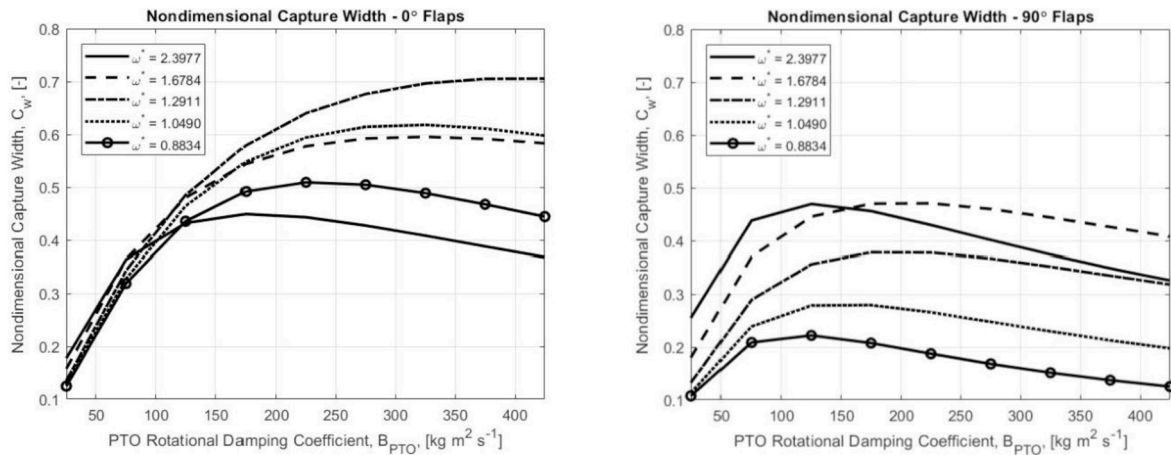


Fig. 13. Relative capture width over a range of PTO damping coefficients for both 0° (left) and 90° (right) flap orientations.

possible explanation for the similarity in transmitted energy between the two flap orientations at the downstream probe in Fig. 14. Another explanation may be that the waves investigated may have been of sufficiently high frequency in which the wave pressure may not penetrate below the solid upper panel, resulting in radiated wave energy that is greater than the energy transmitted. Forced oscillation tests in still water

would help to determine the energy in the radiated waves and will be performed in future work.

The resulting nondimensional wave-induced moment, M_w^* , on the vertically fixed paddle is presented in Fig. 17. The experimental results show that the open-flap configuration can reduce the pitch wave-excitation moment between 15 and 55%. In the range of waves tested

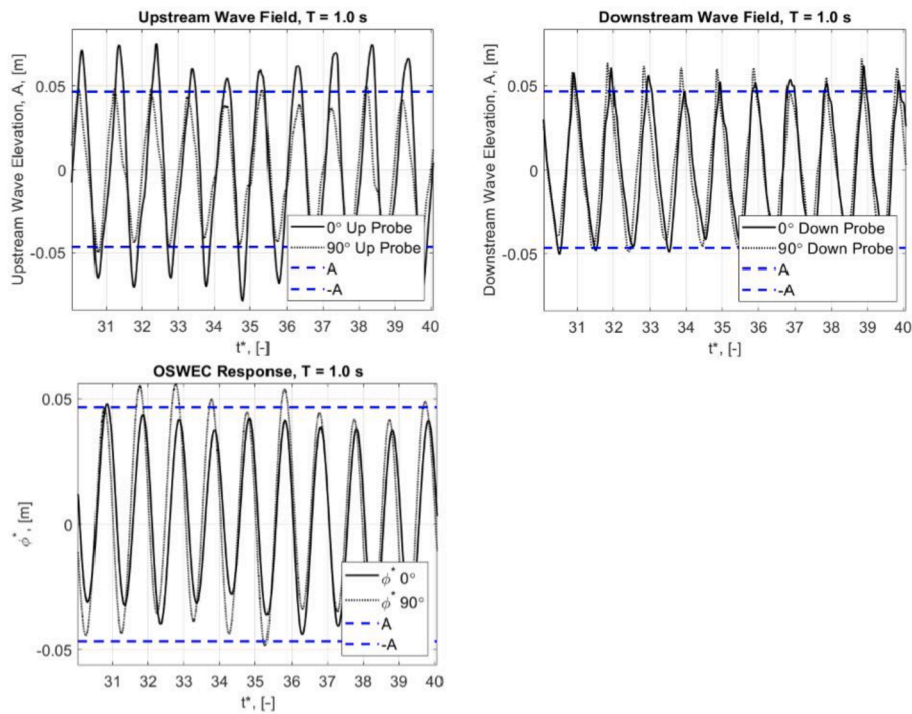


Fig. 14. Time history of upstream (top left) and downstream (top right) wave elevation. Dimensional OSWEC pitch response, $\phi^* = Z_h \tan(\phi)$, (bottom) in waves of $T = 1.0$ s (nondimensional wave frequency of $\omega^* = 1.68$) for the 0° and 90° flap orientations. Time on the x-axis is nondimensionalized by the wave period, T .

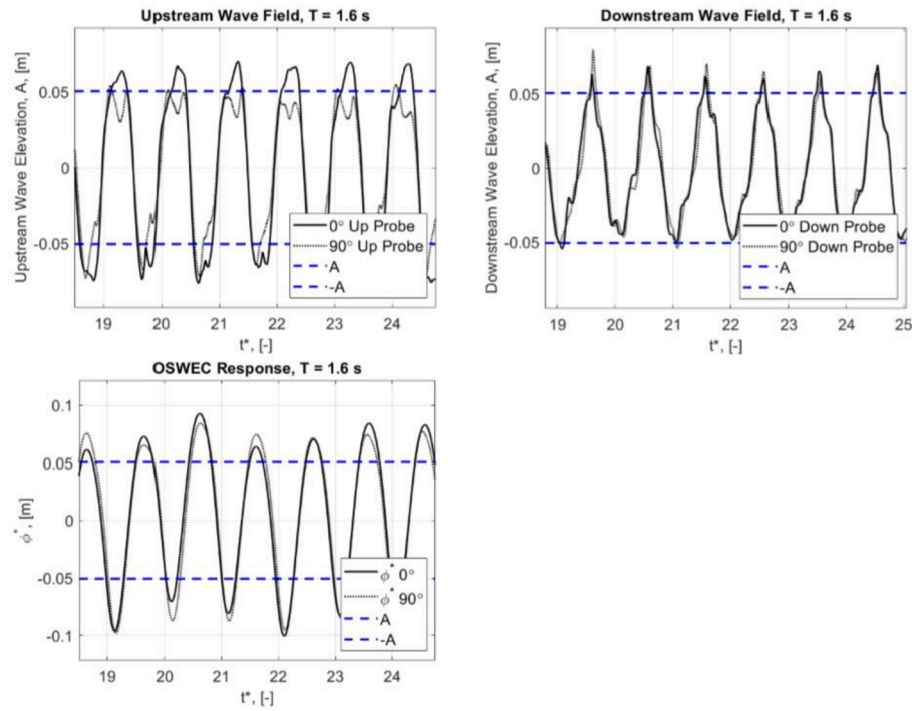


Fig. 15. Time history of upstream (top left) and downstream (top right) wave elevation. Dimensional OSWEC pitch response, $\phi^* = Z_h \tan(\phi)$, (bottom) in waves $T = 1.6$ s (right) (nondimensional wave frequency $\omega^* = 1.05$) for the 0° and 90° flap orientations. Time on the x-axis is nondimensionalized by the wave period, T .

in this experiment, the load shedding capabilities of the flaps became increasingly significant as the angular frequency of the waves decreased which agrees with the numerical results. Storm conditions often lead to waves with longer periods, so this characteristic may result in the OSWEC being capable of operating during more extreme sea states than similar designs without the means of geometrical load shedding

capabilities. The greater load shedding at longer wave periods is in part because of the solid upper panel height above the flap window. Since the dynamic wave pressure associated with the longer wavelengths of the lower frequency waves decay more slowly with depth, and hence can penetrate below the solid panel and through the flap window. The experimental results for 90° flaps agree well with the simulation, and the



Fig. 16. Overtopping sequence for wave period $T = 1.2$ s and wave amplitude $A = 0.07$ m and the device in the 90° flap orientation. Each photo in the sequence is separated by 0.1 s and labeled as its relation to the wave period, T , considering $t = 0$ s to be the time at the paddle’s peak negative pitch rotation for the period shown. Images were recorded at a capture rate of 500 frames per second.

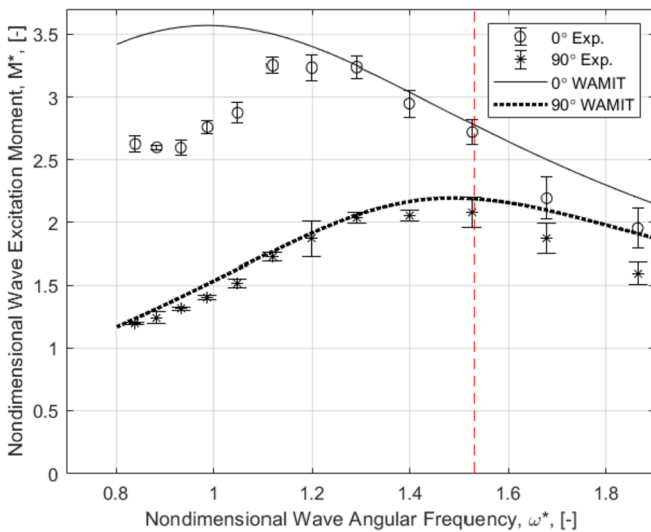


Fig. 17. Comparison of experimental results and WAMIT numerical results of nondimensional wave-induced moment for both 0° and 90° flap orientations. The moments are nondimensionalized by τ_m (see Eq. (6)).

0° flaps for nondimensional frequencies over 1.2. For frequencies at or below 1.2 there is significant deviation from the simulation. This can be potentially be attributable to a cancellation effect arising from the phase difference between the incident and reflected waves (refer to Fig. 18). The phase difference caused during reflection is a function of the frequency as well as localized effects such as the significant vortex shedding observed at the water surface, as no dye or other flow visualization techniques were applied, when water passed the small space between the OSWEC and tank walls in the 0° flap case. Such effects were not significantly observed for the open flap condition. Lastly, the numerical simulations do not consider the dynamics above $z = 0$. In reality, waves overtop the device and this effect is more drastic at lower frequency waves. In the closed-flap case, any energy that is not reflected must flow over the top of the device which will not contribute to the wave induced moment on the paddle. In the open flap-case, some of the incoming

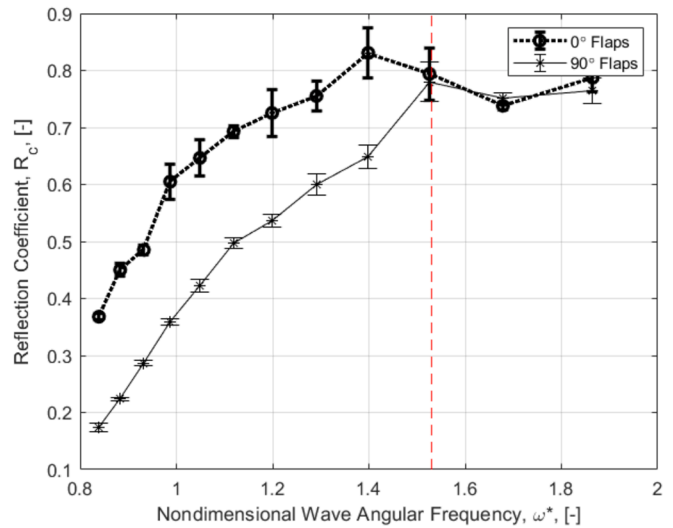


Fig. 18. Reflection coefficient for both 0° and 90° flap orientations where the paddle was fixed in the vertical position.

energy that is not reflected flows through the flap window and the remainder flows over the top, which will be less significant than the closed-flap case. In other words, if energy can pass through the open flap window, there will be less overtopping which is not accounted for in the numerical simulation.

Fig. 18 shows the results for the reflection coefficient obtained from the experiments. The same logic applies that the dynamic wave pressure from the longer waves penetrates below the solid upper panel where the higher frequency waves do not. A clear separation is seen in the plot at $\omega^* = 1.53$ where frequencies at or above this point show no significant difference in reflection between flap orientations, and frequencies below this point show a reduction in reflection up to 53% in the open-flap configuration. This point is represented by dashed vertical lines in Figs. 17 and 18. This point is likely where the wave pressure begins to penetrate the flap window in the fixed case. Fig. 17 also shows significance at this frequency where the moments from waves below this point begin to separate further between the two flap orientations. This highlights the load shedding capabilities further by suggesting that more energy is transmitted past the device in the open flap configuration as touched upon in the results from Fig. 14 above.

7. Conclusions

This paper investigated the performance and load shedding capabilities of an oscillating surge wave energy converter utilizing adjustable flaps as a means of controlling the hydrodynamic loads. The pitch response to waves was measured experimentally for flap orientations of 0° (closed) and 90° (open). The experimental conditions were modeled numerically using WAMIT and WEC-Sim and a good agreement was found between the simulations and experiments. Flap orientation did not have a significant effect on angular displacement of the device in the absence of a PTO, so further numerical simulations were performed to estimate the effect of flap orientation on structural loads and power capture. The numerical results suggest that when partnered with traditional PTO damping control strategies, the adjustable geometry adds another layer of control and tuning capabilities that warrant further optimization studies.

By fixing the paddle in the vertical position, the wave-induced moments on the paddle and reflection coefficients were measured with confidence. These results confirmed the flap orientation can significantly control the loads and energy transfer from waves. Overall, the flaps provide a mechanical means to reduce the loads on the foundation and can be designed to shed loads in case of exceedance of pre-

determined thresholds, improving the design life of a WEC system.

Future updates for this conceptual device include testing in a much larger wave basin in the absence of wall effects and with the ability to generate longer wave periods. It is of interest to observe the model's response to wave periods on both sides of its resonant pitch period and the effect of flap orientation to a wider range of environmental conditions. Repeating free-decay tests in an open basin in the absence of wall effects will allow for a simpler identification of the pitch resonant period and damping ratio in both flap orientations. Testing in a large basin may also assist in identifying the discrepancies between experimental and numerical results seen in Fig. 17. Another option that could be explored is shifting the pitch resonant period by either applying external linear springs to the device or by changing the center of gravity for continued experiments in the wave tank. Updates to the model itself may also investigate the size and location of the flap window and adjusting the mass properties using the ballast ports already constructed. The goal will be to tune the device's hydrodynamics to shift its resonant pitch frequency to match the wave-excitation frequency for maximum power extraction in operational sea states and shed loads in extreme conditions. Options for testing combinations of the adjustable geometry control discussed in this paper with a model PTO system are currently being explored.

Declarations of interest

None

Acknowledgements

The first author acknowledges the support of AVANGRID Foundation, Inc. for the award of a Scholarship for Energy and Environment Postgraduate Studies in the United States. This work was supported by the U.S. Department of Energy under Contract No. DE-AC36-08GO28308 with the National Renewable Energy Laboratory. Funding for the work was provided by the DOE Office of Energy Efficiency and Renewable Energy, Water Power Technologies Office.

The U.S. Government retains and the publisher, by accepting the article for publication, acknowledges that the U.S. Government retains a nonexclusive, paid-up, irrevocable, worldwide license to publish or reproduce the published form of this work, or allow others to do so, for U.S. Government purposes.

References

- Cameron, L., Doherty, R., 2010. Design of the next generation of the Oyster wave energy converter. In: 3rd Int. Conf. Ocean Energy, pp. 1–12.
- Crooks, D., Hoff, J. van 't, Folley, M., Elsaesser, B., 2016. Oscillating wave surge converter forced oscillation tests. In: Vol. 6 Ocean Sp. Util. Ocean Renew. Energy V006T09A021.
- Dean, R.G., Dalrymple, R.A., 1991. *Water Wave Mechanics for Engineers and Scientists*, second ed. World Scientific Publishing Co., New Jersey.
- Gomes, R.P.F., Lopes, M.F.P., Henriques, J.C.C., Gato, L.M.C., Falcão, A.F.O., 2015. The dynamics and power extraction of bottom-hinged plate wave energy converters in regular and irregular waves. *Ocean Eng.* 96, 86–99.
- Henry, A., Rafiee, A., Schmitt, P., Dias, F., Whittaker, T., 2013. The characteristics of wave impacts on an oscillating wave surge converter. *J. Ocean Wind Energy* 1, 101–110.
- Lucas, J., Livingstone, M., Vuorinen, M., Cruz, J., 2012. Development of a wave energy converter (WEC) design tool – application to the WaveRoller WEC including validation of numerical estimates. In: Proc. 4th Int. Conf. Ocean Energy..
- Nallayarasu, S., Fatt, C.H., Jothi Shankar, N., 1995. Estimation of incident and reflected waves in regular wave experiments. *Ocean Eng.* 22, 77–86.
- Ramudu, E., 2011. Ocean wave energy-driven desalination systems for off-grid coastal communities in developing countries. In: Proc. - 2011 IEEE Glob. Humanit. Technol. Conf. GHTC 2011, pp. 287–289.
- Ruehl, K., Michelen, C., Kanner, S., Lawson, M., Yu, Y.H., 2014. Preliminary verification and validation of WEC-sim , an open-source wave energy converter design tool preprint. In: Int. Conf. Ocean. Offshore Arct. Eng. OMAE, pp. 1–8.
- Tom, N.M., Lawson, M.J., Yu, Y.H., Wright, A.D., 2016. Development of a nearshore oscillating surge wave energy converter with variable geometry. *Renew. Energy* 96, 410–424.
- WAMIT Version 7.2 User Manual, 2017.
- Wehausen, J.Y., Laitone, E.V., 1960. Surface waves. *Encycl. Phys.* 9, 446–778.
- Wei, Y., Abadie, T., Henry, A., Dias, F., 2016. Wave interaction with an oscillating wave surge converter. Part II: slamming. *Ocean Eng.* 113, 319–334.
- Wei, Y., Ashkan, R., Henry, A., Dias, F., 2015. Wave interaction with an oscillating wave surge converter, Part I: viscous effects. *Ocean Eng.* 104, 185–203.
- Whittaker, T., Folley, M., 2012. Nearshore oscillating wave surge converters and the development of Oyster. *Philos. Trans. R. Soc. A Math. Phys. Eng. Sci.* 370, 345–364.